Chapter 1
Time-Resolved Tapping-Mode Atomic Force Microscopy

Ali Fatih Sarioglu and Olav Solgaard

Abstract Atomic force microscopy has unprecedented potential for quantitative mapping of material-specific surface properties on the nanoscale. Unfortunately, methods developed for local stiffness measurements suffer from low operational speeds and they require large forces to be applied to the surface, limiting resolution and precluding measurements on soft materials such as polymers and biological samples. On the other hand, tapping-mode AFM, which is well suited to soft materials due to its gentle interaction with the surface, cannot be used to recover information on the tip–sample interaction (and hence, on the material properties) due to limited mechanical bandwidth offered by the resonant AFM probe.

In this chapter, a technique, called Time-resolved Tapping-mode Atomic Force Microscopy, designed for rapid quantitative material characterization on the nanoscale is described. The technique is based on time-resolved measurement of tip–sample interaction forces during tapping-mode AFM imaging by a specially designed micromachined AFM probe. The probe has an integrated high-bandwidth interferometric force sensor that is used to resolve tip–sample interaction forces with high sensitivity and temporal resolution. In the first part of the chapter, the theory, design, and fabrication of the probes are described in detail. Then quantitative force measurements with microsecond time resolution in tapping-mode imaging are presented. Finally, higher harmonic images based on the interaction force measurements are presented for various samples, demonstrating the range of applications of the technique.

1.1 Introduction

Atomic force microscopy (AFM) [1] is one of the main techniques for high-resolution nondestructive measurement of surface topography. Its operation is based on the mechanical interaction of an atomically sharp tip at the end of a flexible cantilever beam with the sample surface. By raster scanning the sharp tip over the sample surface and recording its displacement, AFM provides atomic scale resolution [2] and can be employed in a variety of environments, such as air, vacuum

and liquids, and over wide range of temperatures. The high resolution together with such versatility makes this microscopy technique applicable over a wide range of problems in various disciplines from biology to material science.

Beyond topography measurements, there is an increasing interest in the use of AFM for force measurements and quantitative mapping of local elastic and viscoelastic surface properties. In fact, there are several AFM-based techniques already developed for local mechanical measurements, such as nanoindentation [3], force volume imaging [4], ultrasonic force microscopy [5, 6], pulsed-force microscopy [7, 8], and force modulation microscopy [9, 10]. However, these techniques either require excessive forces to be applied on the surface, limiting their use to stiff materials, or rely on the measurement of a parameter whose value is affected by several processes other than the sample elastic properties, complicating the interpretation of the results of these techniques.

Tapping-mode atomic force microscopy (TM-AFM) [11] is a dynamic imaging technique, in which the probe is oscillated close to its resonance frequency and contacts with the sample briefly once in every oscillation. The cantilever oscillation amplitude is kept constant by the feedback loop, and the feedback signal to the piezoelectric actuator is recorded as a topography image. One of the advantages of the TM-AFM imaging is that it eliminates the continuous tip–sample contact that leads to large frictional forces that may damage both the tip and the sample. This makes this mode especially well suited for imaging of weakly immobilized macromolecules, as well as soft samples such as polymer surfaces and biological samples [12]. Consequently, this technique is one of the most widely used AFM imaging modes.

In addition to being a popular technique for topography measurements, TM-AFM can be used for compositional mapping of surfaces by recording the cantilever phase [13, 14]. In fact, TM-AFM offers unique advantages for quantitative material characterization. The dynamic interaction forces between the tip and the sample contain important information on adhesive and elastic properties of the surface. Therefore, measurement of interaction forces is a more direct method for material characterization. Measurement of tip–sample interaction forces have been demonstrated by recording the higher harmonics of the cantilever oscillations [15, 16]. Unfortunately, these measurements suffer from low signal-to-noise ratio mainly due to the limited mechanical bandwidth of the resonant cantilever in TM-AFM. Recently, several techniques have been introduced to increase the SNR in measurements of the higher frequency components of the tip–sample interaction forces. These developments can be summarized as engineering the cantilever frequency response by designing special cantilever geometries [17, 18], driving the cantilever at its multiple eigenmodes simultaneously [19], employing fast and wide-bandwidth membrane-based probes [20, 21] and using specialized cantilevers with off-axis tip to utilize the higher frequency torsional mode [22, 23]. In this chapter, we focus on direct measurement of the nonlinear tip–sample interaction forces in TM-AFM using AFM probes with integrated high-bandwidth interferometric force sensors that offer increased temporal resolution [24, 25]. These probes combine the advantages of TM-AFM imaging and AFM force spectroscopy in a single device. They are unique in the sense that

high temporal resolution in force measurements is contributed by the reduced mass of the force sensor. In addition, the integrated differential interferometric sensor enables independent measurement of cantilever motion and interaction force by minimizing crosstalk between cantilever oscillations and tip motion.

The organization of the chapter is as follows: In Sect. 1.2, the tip–sample interaction forces are explained using analytical models (Sect. 1.2.1) and the mechanical response of a typical AFM probe is discussed (Sect. 1.2.2). In Sect. 1.3, we introduce an AFM probe that is developed to measure the interaction forces in TM-AFM with an interferometric high-bandwidth force sensor. First, the dynamics of the probe in TM-AFM is simulated using analytical models (Sect. 1.3.1). The design and operating principles together with the details of microfabrication process is explained in detail (Sect. 1.3.2–1.3.4). Next, the detection techniques, characterization results, and calibration procedures for quantitative force measurements are presented. (Sects. 1.3.5 and 1.3.6) Finally, the section is concluded with the experimental force measurement results (Sect. 1.3.7). In Sect. 1.4, the compositional mapping of various surfaces by utilizing the higher harmonics of the measured tip–sample interaction forces is demonstrated. Specifically, high-bandwidth harmonic imaging results of a checkerboard test sample (Sect. 1.4.1), self-assembled monolayer (SAM) of alkanethiols on gold surface (Sect. 1.4.2) and SBS triblock copolymer film (Sect. 1.4.3) are demonstrated. Finally, the chapter is concluded with a summary and discussion in Sect. 1.5.

1.2 Tip–Sample Interactions in TM-AFM

In the following section, first, the tip–sample interaction forces in TM-AFM are explained using analytical models and the mechanical response of a typical AFM probe under these forces is discussed.

1.2.1 Interaction Forces in TM-AFM

The tip–sample interactions in TM-AFM are dynamic in nature due to the oscillatory motion of the probe [26]. When the tip and sample are close, but not in contact, the tip is pulled towards the sample by long-range attractive forces. These forces originate due to Van der Waals interaction and are relatively weak. On the other hand, as the tip makes contact with the surface, the tip is pushed away by elastic forces that arise due to surface indentation. Therefore, in every cantilever oscillation period, the tip traverses both the attractive and repulsive force regimes.

In this chapter, to model the tip–sample interaction, we use the Dejarguin–Muller–Toporov (DMT) contact model [27, 28]. In this model, the AFM tip and the sample surface are modeled as a sphere and a flat half-space, respectively. At large tip–sample distances, the attractive forces between the tip and the sample surface are

derived from the Van der Waals energy. For the geometry of an interacting sphere and a flat surface, the Van der Waals force is given by

$$F_{\text{att}} = \frac{-HR}{6z^2}. \tag{1.1}$$

In this expression, H is the Hamaker constant, R is the radius of curvature of the AFM tip, and z is the distance between the tip and the sample surface.

As the tip approaches and contacts with the sample, repulsive forces emerge in addition to attractive forces. These shorter range forces originate from Pauli and ionic interactions between atoms. In the DMT model, Van der Waals forces between the two bodies are assumed to be constant when the tip–sample distance is smaller than a certain parameter referred as the intermolecular distance. In addition, the repulsive forces are modeled as elastic forces occurring between two bodies due to Hertz contact theory [29]. By combining these two effects, the total interaction force in the repulsive regime is given by

$$F_{\text{rep}} = -\frac{HR}{6a_0^2} + \frac{4}{3}E^*\sqrt{R}d^{3/2}. \tag{1.2}$$

In Eq. (1.2), a_0 is the intermolecular distance, d is the sample indentation and E^* is the reduced Young's modulus of the tip–sample contact. The reduced Young's modulus of the tip–sample contact is given by [29]

$$E^* = \left[\frac{1-\upsilon_{\text{t}}^2}{E_{\text{t}}} + \frac{1-\upsilon_{\text{s}}^2}{E_{\text{s}}}\right]^{-1}, \tag{1.3}$$

where E_{t} (E_{s}) and υ_{t} (υ_{s}) are the tip (sample) Young's modulus and Poisson ratio, respectively.

1.2.2 Cantilever Dynamics and Mechanical Bandwidth in TM-AFM

In this section, we analyze the frequency response of an AFM probe when operated in TM-AFM and discuss the limitations imposed by the probe mechanical bandwidth on the measurements of tip–sample interaction forces. As mentioned before, in TM-AFM the tip interacts with the surface repeatedly at a rate close to the cantilever resonance frequency. Therefore, in steady state, the tip–sample interaction force waveform is treated as a periodic signal and can be expressed as a Fourier series.

$$F_{\text{ts}}(t) = \frac{1}{2}a_0 + \sum_{n=1}^{\infty} a_n \cos(n\omega t) + b_n \sin(n\omega t), \tag{1.4}$$

where the Fourier coefficients are given by

$$a_n = \frac{\omega}{\pi} \int_{-\frac{\pi}{\omega}}^{\frac{\pi}{\omega}} F_{\mathrm{ts}}(t) \cos(n\omega t) \mathrm{d}t, \tag{1.5}$$

$$b_n = \frac{\omega}{\pi} \int_{-\frac{\pi}{\omega}}^{\frac{\pi}{\omega}} F_{\mathrm{ts}}(t) \sin(n\omega t) \mathrm{d}t. \tag{1.6}$$

In the Fourier series of the tip–sample interaction signal, the higher harmonics at the integer multiples of the cantilever drive frequency are due to nonlinearity in the tip–sample interaction discussed in the previous section.

It follows from the discussion above that time-resolved measurements of tip–sample interaction forces in TM-AFM requires a mechanical bandwidth that covers the higher harmonics of the interaction force at the integer multiples of the drive frequency. However, the mechanical response of a resonant AFM cantilever is inherently limited beyond its fundamental resonance frequency. This limitation can be understood from an analysis of the cantilever transfer function.

Figure 1.1 shows the frequency response of a typical rectangular AFM cantilever calculated using analysis (FEA). In this plot, the vertical axis is the displacement gain, which is defined as the ratio of tip displacement amplitude to its DC response, whereas the horizontal axis is the frequency. The peaks in the displacement gain are due to fundamental and higher order flexural resonances of the cantilever. From the plot, we see that below its fundamental resonance frequency, the probe has a flat band response, whereas the mechanical response of the cantilever beam is significantly reduced beyond its fundamental resonance frequency except in close vicinity to higher order modes. As a result, higher harmonics of the periodic interaction force signal are lost unless they are in the close vicinity of higher order resonances and tip–sample interaction forces cannot be fully recovered from the cantilever displacement.

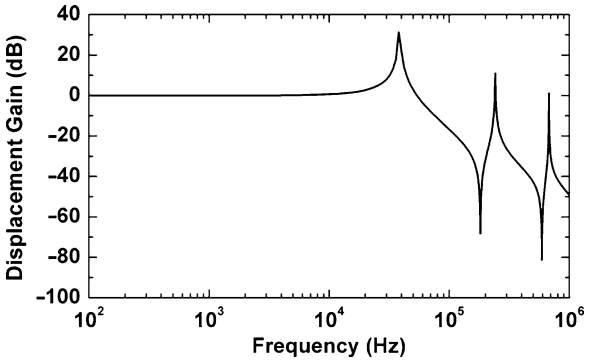

Fig. 1.1 Simulated mechanical response of a typical rectangular AFM cantilever. The cantilever is 300-μm long, 60-μm wide, and 2.5-μm thick and is made of single crystal silicon

Note that the limited bandwidth of TM-AFM is a result of the cantilever being driven on resonance. In fact, forces between an AFM tip and the sample surface can be measured from the displacements of the cantilever when tip–sample interaction force spectrum is band limited within the flat band of the cantilever. Therefore, when the AFM cantilevers are used for force measurement applications, they are either operated statically, or the dynamic interaction rate is kept well below the cantilever resonance frequency. However, these techniques sacrifice the advantages of a resonant probe such as speed, gentle tip–sample interaction, and tip-limited spatial resolution.

1.3 AFM Probes with Integrated Interferometric High Bandwidth Force Sensors

In the previous section, we discussed the potential benefits of measurement of tip–sample interaction forces in TM-AFM. We also pointed out that measurement of these forces remains a difficult challenge due to the limited mechanical bandwidth of conventional AFM probes operated in TM-AFM mode.

In this section, we discuss a new type of AFM probe [24, 25] that can quantitatively measure the interaction forces between the tip and the sample surface during TM-AFM imaging. This probe has an integrated high-bandwidth force sensor that provides the necessary temporal resolution for time-resolved force measurements. To gain insight into the operation of these probes, first the probe is modeled as a coupled damped harmonic oscillator system. Using the tip–sample contact model described in Sect. 1.2.1, the probe dynamics in TM-AFM operation is simulated, and the design principles are explained. In particular, important aspects of mechanical and optical designs are illuminated. In the following sections, the microfabrication process used in realizing these probes is described. The finished probes are characterized and procedures for calibration are explained. Finally, the section is concluded by presenting time-resolved force measurements.

The geometry of the AFM probe with an integrated high-bandwidth force sensor is shown in Fig. 1.2. The probe is mainly composed of a rectangular cantilever beam and an interferometric force sensor. The force sensor is a diffraction grating at the end of the cantilever beam. The sharp tip resides at the very end of the force sensor and is coupled to a stiff and small mechanical resonator that is a part of the diffraction grating. This tip-coupled resonator is much smaller and stiffer than the cantilever beam and therefore has a higher mechanical bandwidth than the soft and massive cantilever beam. As a result, the resonator remains mechanically responsive to the high frequency components of the nonlinear tip–sample interaction forces where the response of the resonant cantilever is limited. Consequently, the tip–sample interaction forces can be obtained through the relative displacement of this resonator with respect to the cantilever beam.

This probe structure combines the advantages of TM-AFM imaging and AFM force spectroscopy in a single device. Specifically, the resonant cantilever

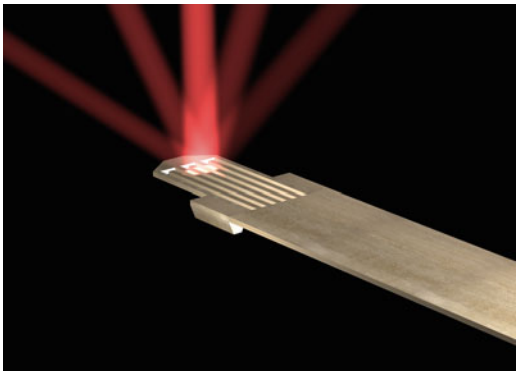

Fig. 1.2 A computer drawing showing the geometry of our AFM probe with an integrated force sensor. The probe is illuminated with a laser beam and the resulting diffraction pattern is also indicated

component provides gentle tip–sample interaction and high resolution as in TM-AFM, whereas the force sensor operated below its resonance can provide quantitative time-resolved measurements of tip–sample interaction forces.

1.3.1 Model

Damped harmonic oscillator models have been widely used to describe probe mechanics in TM-AFM [30–37]. When combined with a tip–sample contact model, these models have proved to be useful in understanding basic characteristics of cantilever motion and tip–sample interactions. In this section, using similar models, we show that with the addition of a high-bandwidth force sensor to an AFM probe, it is possible to measure the tip–sample interaction forces with high temporal resolution.

The model to simulate the dynamics of the probes with high bandwidth force sensors consists of two damped harmonic oscillators coupled to each other. A schematic of the model together with the assumed coordinate system is shown in Fig. 1.3. To simulate TM-AFM operation, the cantilever (the larger mass) is excited with a sinusoidal force at a frequency close to the system's fundamental resonance frequency. On the other hand, the forces due to periodic tip–sample interaction acts on the high-bandwidth force sensor (smaller mass). The equations of motion for the system can be written as:

$$m_{\mathrm{c}}\frac{\partial^2 z_{\mathrm{c}}}{\partial t^2} = -k_{\mathrm{c}}z_{\mathrm{c}} - \gamma_{\mathrm{c}}\frac{\partial z_{\mathrm{c}}}{\partial t} - k_{\mathrm{s}}\left(z_{\mathrm{c}} - z_{\mathrm{s}}\right) - \gamma_{\mathrm{s}}\left(\frac{\partial z_{\mathrm{c}}}{\partial t} - \frac{\partial z_{\mathrm{s}}}{\partial t}\right) + F_{\mathrm{dr}}, \tag{1.7}$$

$$m_{\mathrm{s}}\frac{\partial^2 z_{\mathrm{s}}}{\partial t^2} = -k_{\mathrm{s}}\left(z_{\mathrm{s}} - z_{\mathrm{c}}\right) - \gamma_{\mathrm{s}}\left(\frac{\partial z_{\mathrm{s}}}{\partial t} - \frac{\partial z_{\mathrm{c}}}{\partial t}\right) + F_{\mathrm{ts}}, \tag{1.8}$$

$$\gamma_{\mathrm{c}} = m_{\mathrm{c}}\frac{\omega_{0\mathrm{c}}}{Q_{\mathrm{c}}}, \tag{1.9}$$

$$\omega_{0\mathrm{c}} = \sqrt{\frac{k_{\mathrm{c}}}{m_{\mathrm{c}}}}, \tag{1.10}$$

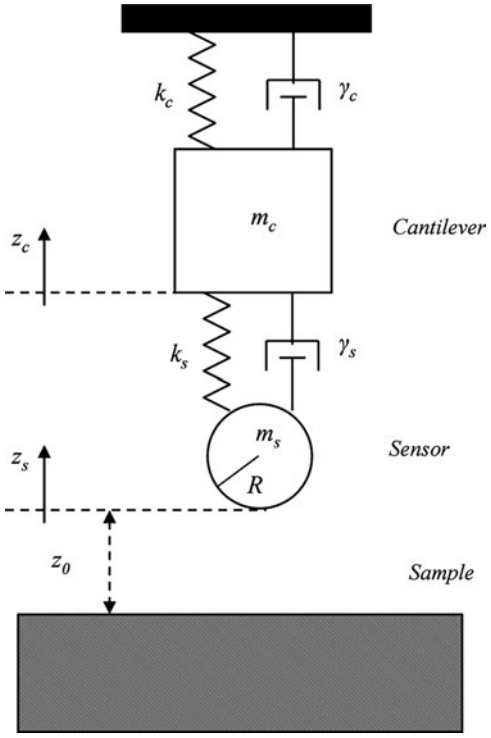

Fig. 1.3 Coupled damped harmonic oscillators used to model the operation of a probe with an integrated high-bandwidth force sensor in TM-AFM imaging

$$\gamma_s = m_s \frac{\omega_{0s}}{Q_s}, \tag{1.11}$$

$$\omega_{0s} = \sqrt{\frac{k_s}{m_s}}. \tag{1.12}$$

In these equations, m_c (m_s), z_c (z_s), γ_c (γ_s), k_c (k_s) and Q_c (Q_s) are the effective mass, instantaneous position, damping coefficient, spring constant, and quality factor of the cantilever beam (force sensor), respectively. In addition, ω is the drive frequency, while ω_{0c} (ω_{0s}) is the fundamental resonance frequency of the cantilever (force sensor). F_{dr} is the driving force applied to the cantilever and F_{ts} is the tip–sample interaction force acting on the force sensor. In the calculations, the tip–sample interaction forces are modeled using the DMT contact model described in Sect. 1.2.1 and is given by

$$F_{ts} = \begin{cases} \frac{-HR}{6(z_0+z_c)^2} & z_0 + z_c \geq a_0 \\ -\frac{HR}{6a_0^2} + \frac{4}{3}E^*\sqrt{R}\,(a_0 - z_0 - z_c)^{3/2} & z_0 + z_c < a_0 \end{cases}, \tag{1.13}$$

By solving (1.7)–(1.13) using numerical methods, the cantilever and force sensor positions are calculated as a function of time. Using these results, the

Table 1.1 Parameters used for TM-AFM calculations for a probe with a high-bandwidth force sensor

Parameter	Value	Parameter	Value
m_c	1×10^{-7} g	F_{dr}	10^{-8} N
k_c	10 N/m	H	5×10^{-20} J
m_s	1×10^{-9} g	z_0	3.5×10^{-8} m
k_s	1,000 N/m	R	10×10^{-9} m
Q_c	100	a_0	1×10^{-10} m
Q_s	100	E_t	1.29×10^{11} Pa
ω_{0c}	1×10^4 rad/s	υ_t	0.28
ω_{0s}	1×10^6 rad/s	E_s	100×10^9 Pa
ω	9.855×10^3 rad/s	υ_s	0.3

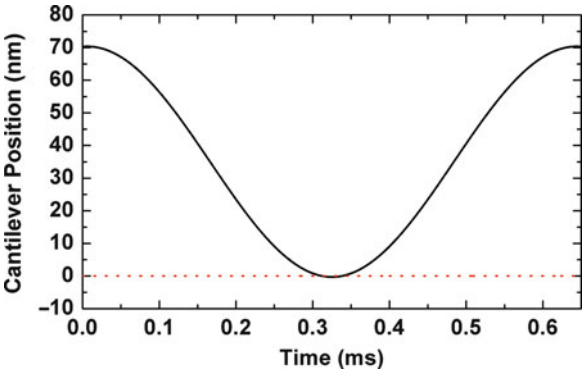

Fig. 1.4 Calculated position of the cantilever with the integrated force sensor. The *red dotted line* indicates the sample surface position

time-dependent interaction forces between the sensor and the sample surface are calculated. The values of the model parameters used for these calculations are listed in Table 1.1. Note from the table that the force sensor mass is assumed to be much smaller than the cantilever mass, while the sensor spring constant is chosen much larger than the cantilever spring constant. This ensures that the resonance frequency of the force sensor is higher than the fundamental resonance frequency of the system and results in a higher force sensor mechanical bandwidth.

Figures 1.4 and 1.5 show the calculated positions of cantilever and force sensor, respectively after the system reaches steady-state for a single oscillation period. The simulation results show that the force sensor closely follows the cantilever motion for most of the oscillation period. This is due to the fact that the drive frequency is well below the resonance frequency of the force sensor, and therefore, the force sensor is in phase with the cantilever motion. However, a close-up of the response of the system in the vicinity of tip–sample contact (shown in Fig. 1.6) shows that this synchronization between cantilever and force sensor oscillations is lost during the tip–sample interaction. This can be explained as follows. The tip–sample

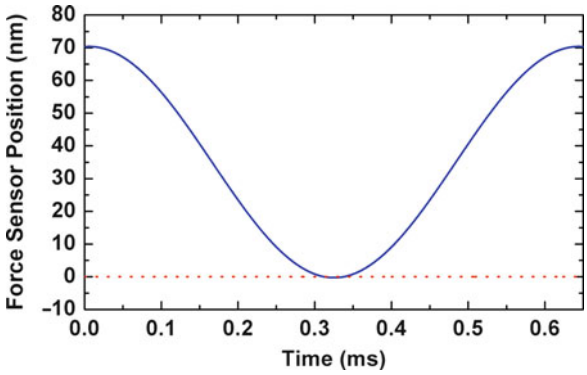

Fig. 1.5 Calculated position of the force sensor position. The *red dotted line* indicates the sample surface position

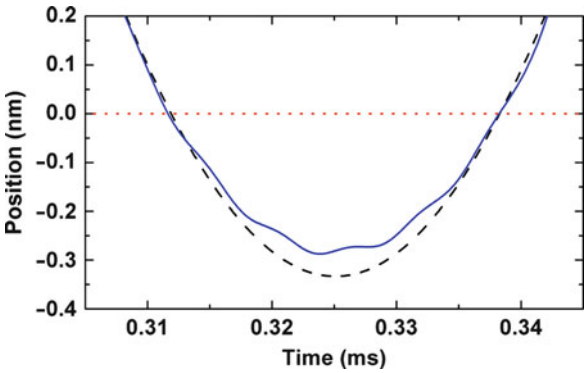

Fig. 1.6 Calculated positions of the cantilever (*black dashed line*) and the force sensor at times close to the tip–sample contact. The *red dotted line* indicates the sample surface position

interaction is nonlinear and therefore introduces higher frequency harmonics into the system as we have discussed in Sect. 1.2. In the simulated model, these forces act directly on the force sensor and are then transferred to the cantilever. Consequently, designed with a higher resonance frequency, the force sensor can capture a number of higher harmonics of the interaction force within its flat band spectrum and displace in response to nonlinear interaction forces. In contrast, the resonantly driven cantilever has a limited response at higher frequencies as we have discussed before, and cannot respond to the interaction forces.

Simulation results show that the relative motion of the force sensor with respect to the cantilever is sensitive to the interaction forces, so the differential motion provides a way to recover the tip–sample force in TM-AFM. Specifically, the interaction forces can be found by simply multiplying the relative displacement of the force sensor ($z_s - z_c$) by the spring constant of the force sensor (k_s). Figure 1.7 shows the simulated tip–sample interaction forces (black dashed line) together with the

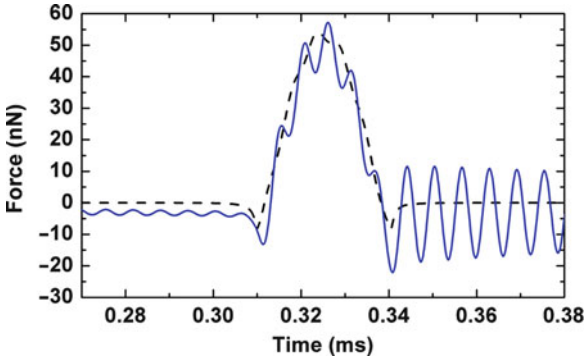

Fig. 1.7 Simulated tip–sample interaction force (*black dashed line*) and tip–sample interaction force, estimated based on the force sensor displacement relative to the cantilever (*blue line*)

estimated force (blue) based on the differential sensor displacement. The estimated force signal fits the actual tip-sample interaction force quite well, except that it adds high frequency oscillations that are due to under-damped nature of the force sensor. The oscillations are triggered by the interaction force high frequency harmonics that are close to sensor resonance frequency. They are more pronounced with the increasing quality factor of the force sensor. This result also indicates that the force sensor acts as a mechanical amplifier for certain harmonics of the interaction force and this can be utilized for higher harmonic imaging as will be discussed in Sect. 1.4. The disadvantage of this ringing effect, however, is that it distorts the force measurements and complicates calibration, so it should be corrected. This can be achieved with the knowledge of the force sensor transfer function, as will be discussed in Sect. 1.3.7.

To summarize, using a simple harmonic oscillator model, we have shown that an integrated high-bandwidth force sensor on the cantilever solves the problem of limited mechanical bandwidth in TM-AFM and provides improved temporal resolution to resolve the interaction forces.

1.3.2 Interferometric Grating Sensor

In the actual probe geometry (shown in Fig. 1.2), the large and small masses correspond to cantilever beam and the tip-coupled force sensor at the end, respectively. In order to measure the differential tip-cantilever displacement, an interferometric grating displacement sensor [38–40] is used. The grating sensor is designed such that the tip is mechanically coupled to alternating grating fingers, while the rest of the grating fingers are isolated from each other and remain free. Therefore, when there is force acting on the tip, the tip-coupled fingers displace relative to the rest of the fingers. To demonstrate the force sensor operation, the sensor response under the

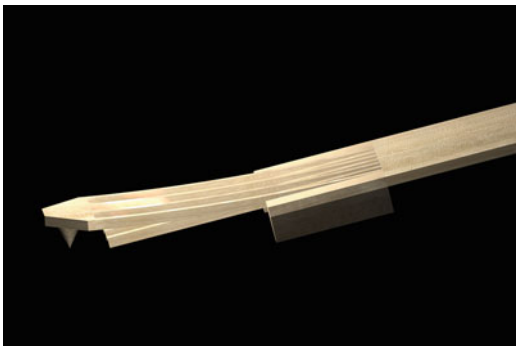

Fig. 1.8 Computer drawing showing the response of the force sensor when the tip interacts with the surface

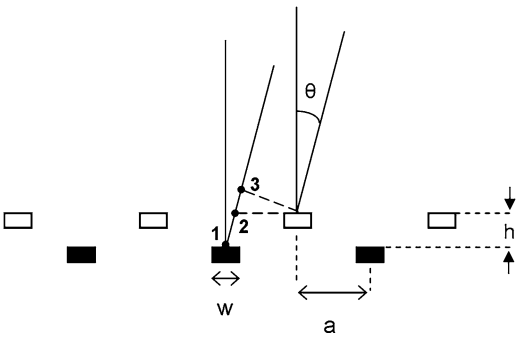

Fig. 1.9 Schematic of the cross section of the differential interferometric grating sensor. The moving (reference) fingers are represented by *bright* (*dark*) features

effect of a tip-sample force is depicted in Fig. 1.8, where the relative displacement is exaggerated to clarify the concept.

In operation, the differential grating sensor is illuminated with a focused laser beam and the reflected light forms a diffraction pattern. Modeling of the sensor operation requires the calculation of the diffracted light intensity pattern as a function of relative vertical displacement between the moving and reference finger sets. For this purpose, the sensor is treated as a two set of mirror surfaces that are vertically displaced as shown in Fig. 1.9. For a grating that is composed of N identical fingers of width w with a period of $2a$, the wave amplitude at the far field is calculated using Fraunhofer integral [41] and is given by

$$\Psi(\theta) \propto \left[\frac{\sin(\pi w \cos\alpha \sin\theta/\lambda)}{\pi w \cos\alpha \sin\theta/\lambda}\right]\left[\frac{1-\exp(-\mathrm{i}4\pi N a \cos\alpha \sin\theta/\lambda)}{1-\exp(-\mathrm{i}4\pi a \cos\alpha \sin\theta/\lambda)}\right]. \quad (1.14)$$

The first part of this expression gives the amplitude of the diffracted wave for a single infinitely long finger of width w as a function of the diffraction angle, whereas the second part is due to the interference of the reflected waves from the periodic grating fingers. Note that, (1.14) also includes the effect of an incident angle α along the grating fingers, since in practical implementation of optical lever, this angle is never zero. The grating sensor can be considered to be formed of two such gratings, namely the moving and reference gratings that are displaced in the vertical

direction. Therefore, to calculate the total diffracted field Ψ_t, the diffracted wave amplitudes from both moving fingers and reference fingers should be added. Note that the reflected waves due to moving and reference finger sets are identical except for the phase difference due to height offset between the two finger sets. Therefore, the total diffracted wave amplitude can be expressed as

$$\Psi_t(\theta) = \Psi(\theta) + \Psi(\theta)\, e^{i\Omega(\theta)}. \tag{1.15}$$

The phase difference Ω is a function of the diffraction angle and it is calculated by multiplying the wave number by the optical path difference between the two waves and is expressed as

$$\Omega = \frac{2\pi}{\lambda} \cos\alpha \left[h + \ell_{12} + \ell_{23}\right]. \tag{1.16}$$

where α is the incident angle along the grating fingers and h is the vertical height difference between the finger sets. ℓ_{12} and ℓ_{23} are the distances between points (1,2) and (2,3) from Fig. 1.9, respectively, and are given by

$$\ell_{12} = \frac{h}{\cos\theta}, \tag{1.17}$$

$$\ell_{23} = [a - h\tan(\theta)]\sin\theta. \tag{1.18}$$

Substituting (1.17) and (1.18) in (1.16), the phase difference between the waves reflected from moving and reference fingers is given by

$$\Omega = \frac{2\pi}{\lambda} h \cos\alpha \left[(1 + \cos\theta) + (a/h)\sin\theta\right]. \tag{1.19}$$

The total diffracted wave amplitude is calculated using (1.14) and (1.15) and is given by

$$\Psi_t(\theta) \propto \left[\frac{\sin(\pi w \cos\alpha \sin\theta/\lambda)}{\pi w \cos\alpha \sin\theta/\lambda}\right]\left[\frac{1-\exp(-i4\pi N a \cos\alpha \sin\theta/\lambda)}{1-\exp(-i4\pi a \cos\alpha \sin\theta/\lambda)}\right][1+\exp(i\Omega)]. \tag{1.20}$$

The diffracted light intensity as a function of the diffraction angle is calculated by the magnitude square of the wave amplitude given in (1.20) and is expressed as

$$I(\theta) \propto \left[\frac{\sin\left[(\pi w \cos\alpha \sin\theta)/\lambda\right]}{(\pi w \cos\alpha \sin\theta)/\lambda}\right]^2 \left[\frac{\sin\left[(N\pi 2a \cos\alpha \sin\theta)/\lambda\right]}{\sin\left[(\pi 2a \cos\alpha \sin\theta)/\lambda\right]}\right]^2 \cos^2\left(\frac{\Omega}{2}\right). \tag{1.21}$$

In this expression, the first term is the light intensity due to single grating finger, the second term is due to the interference of the reflected waves from multiple grating fingers and the final term is due to the interference of the reflected waves from the moving and reference finger sets. This formulation is compact and simple to evaluate numerically, but the fact that Ω is a function of θ, makes it hard to interpret.

For a formulation that separates diffraction angle and phase shift, and therefore is easier to interpret, see Ref. [42].

Using (1.21), the diffracted light intensities as a function of diffraction angle are calculated for a set of finger displacements. In the calculations, it is assumed that the grating has three finger pairs. Both the moving and reference grating fingers are 3 μm wide and the gap between the adjacent fingers is 3 μm. The grating is illuminated with a plane wave with a wavelength of 670 nm with a 0° incidence angle. In Fig. 1.10, the calculated far-field diffraction patterns for three different values of finger displacement are presented. The light intensities are normalized to the maximum intensity of the zeroth order. From these plots, it is observed that when there is no vertical displacement between the two finger sets, the diffraction pattern is composed of the specular reflection of the fingers as the dominant order (also called zeroth diffraction order) together with higher order modes that are called even modes. As one of the finger sets displaces with respect to another, some of the light intensity is partially transferred to new diffraction orders which are referred as odd orders. As the distance between the two finger sets reaches $\lambda/4$, where λ is the wavelength of laser illumination, the light intensity at the odd orders are maximized whereas the light intensities at the even orders including the zeroth order are minimized.

In order to calculate the light intensity of a particular diffraction order as a function of vertical finger displacement, the diffraction angles that correspond to the even and odd diffraction orders are determined using

$$2a \sin\theta \cos\alpha = m\lambda, \tag{1.22}$$

where m is an even (odd) integer for even (odd) orders. Substituting (1.22) in (1.19) and assuming a small diffraction angle, the phase difference between the lights reflected from the moving and reference fingers corresponding to a particular diffraction order can be expressed as

$$\Omega_m = \frac{2\pi}{\lambda} h \left[2\cos\alpha + (m\lambda/2h)\right]. \tag{1.23}$$

Using (1.23) in (1.21), the relation between the light intensity of a particular diffraction order and vertical displacement between the moving and reference finger sets can be expressed as

$$I_{\text{even}} \propto \cos^2\left(\frac{2\pi}{\lambda} h\cos\alpha\right), \tag{1.24}$$

$$I_{\text{odd}} \propto \sin^2\left(\frac{2\pi}{\lambda} h\cos\alpha\right). \tag{1.25}$$

Figure 1.11 shows the calculated normalized light intensities in the zeroth and first diffraction orders as a function of finger displacement for the grating of Fig. 1.10, when the sensor is illuminated in normal direction. The light intensities in adjacent

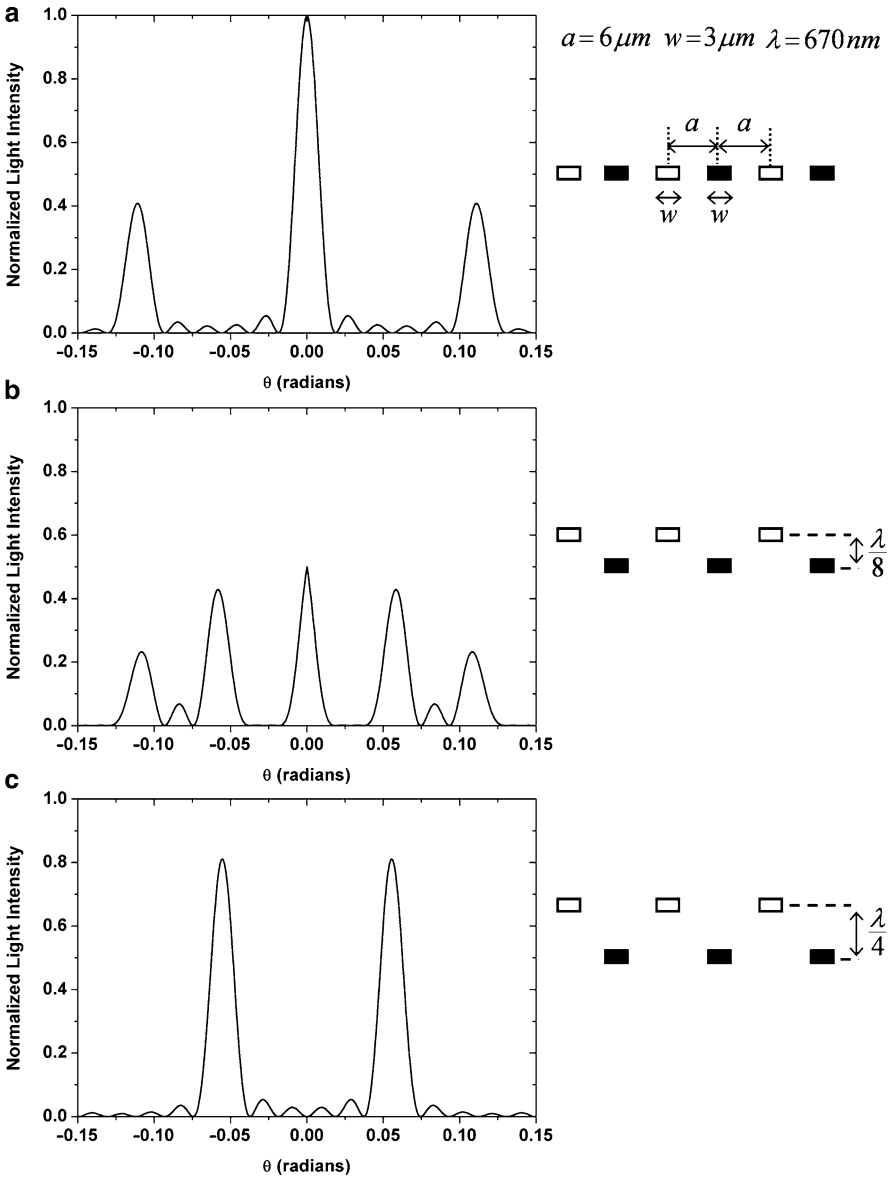

Fig. 1.10 Calculated far field diffracted light intensities as a function of diffraction angle (*left*) for various relative displacements of grating sensor moving and reference finger sets (*right*). Light intensity calculations are performed for three cases with (**a**) no relative displacement, (**b**) a displacement of $\lambda/8$, and (**c**) a displacement of $\lambda/4$, with λ being the wavelength of illumination

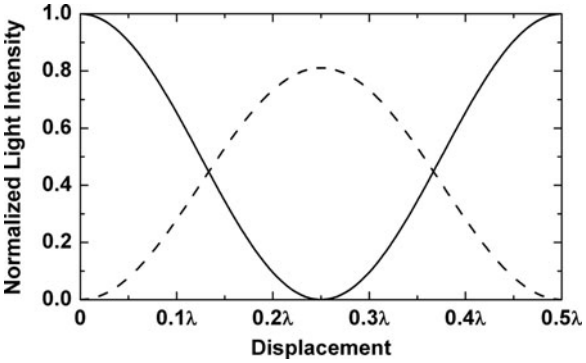

Fig. 1.11 Normalized diffracted light intensities at the zeroth order (*solid line*) and at the first order (*dashed line*) as function of vertical displacement between the grating finger sets. This result is for a grating with 50% duty cycle, i.e., $w/a = 0.5$

diffracted orders change in opposite directions as a function of finger displacement, so differential measurement of zeroth and first diffraction order light intensities, together with the total intensity, enable measurement of relative tip displacement with respect to the cantilever body.

An important design criterion for the differential grating sensor is its sensitivity. In the grating sensor, the finger displacement is measured by recording the light intensity at the diffracted orders using a photodiode. Therefore, the sensitivity of the grating sensor can be defined as $|\partial I/\partial h|$ (i.e., absolute light intensity change at a diffraction order for a unit vertical finger displacement). Using (1.24) and (1.25), the change in the intensity of even and odd diffraction orders are given by

$$\left|\frac{\partial I_m}{\partial h}\right| \propto \sin\left(\frac{4\pi}{\lambda} h \cos\alpha\right), \tag{1.26}$$

From (1.26), the displacement sensitivity of the differential grating sensor varies with the finger displacement. Furthermore, the highest displacement sensitivity is achieved when the fingers are displaced by an odd integer multiple of $\lambda/8$. This height offset also ensures that the sensor operates as linearly as possible since $\left|\partial^2 I_m/\partial h^2\right|$ (i.e., the sensitivity change as a function of displacement) is minimized. Consequently, to achieve force measurements with maximum sensitivity and linearity, the grating sensor should have an initial one-eighth of a wavelength height offset between the reference and moving finger sets. Considering the fact that we use a 670-nm laser diode in our experiments and the cantilever is illuminated with a 10° incidence angle in an AFM system with optical lever detection, we design our interferometric grating sensors such that there is an initial height offset of 85 nm between the reference and moving finger sets.

Another important factor in designing differential grating sensor is the separation of diffraction orders so that the light intensities at each order do not interfere with each other and can be measured individually. In order to ensure this, the separation

of the diffracted orders and their optical-beam width on the observation plane should be taken into account. We define the beam width of a diffracted order w_{diff} as the distance between the first two locations with zero light intensity on each side of the maximum intensity point. From (1.21), the beam width w_θ of a diffraction order in angular space can be expressed as

$$w_\theta = \frac{\lambda}{aN\cos\alpha}, \tag{1.27}$$

where N is the number of finger pairs and a is the distance between two adjacent reference and moving fingers. In addition, the angular spacing (i.e., angle difference between the center locations with maximum light intensity) between the zeroth- and first-order diffraction orders is given by

$$s_\theta = \frac{\lambda}{2a\cos\alpha}. \tag{1.28}$$

From (1.27) and (1.28), the ratio of spacing to beam width is given by

$$\frac{s_\theta}{w_\theta} = \frac{\lambda/2a\cos\alpha}{\lambda/aN\cos\alpha} = \frac{N}{2}. \tag{1.29}$$

For the diffracted orders to be well separated, the separation between the orders should be at least as large as the diffracted order beam width. Therefore, from (1.29), it is required that $N \geq 2$. In our probe design, we chose N to be 3 so that the separation of the diffracted orders is ensured. The number of finger pairs is limited due to mechanical considerations and lithography limitations of fabrication process.

1.3.3 Sensor Mechanical Response & Temporal Resolution

The temporal resolution of interaction force measurements with our probes depends on the mechanical bandwidth, and hence, the fundamental resonance frequency of the gating force sensor. In TM-AFM, the tip–sample interaction occurs periodically at a rate close to the cantilever fundamental resonance frequency. Therefore, the ratio of grating sensor resonance frequency to the cantilever resonance frequency is an important design parameter that determines the relative temporal resolution within the probe oscillation period in TM-AFM imaging.

As mentioned before, the tip–sample interaction force waveform strongly depends on the elastic properties of the sample. Specifically, with increasing Young's modulus, the tip–sample contact occurs in a smaller fraction of the cantilever oscillation cycle. [30] Therefore, tip–sample forces on a stiff sample require higher temporal resolution for interaction force measurements than a compliant sample. This means that as the sample gets stiffer, the ratio of force sensor resonance

frequency to cantilever resonance frequency should be increased for accurate force measurements [43].

In our devices, the ratio of sensor resonance frequency to cantilever resonance frequency can be tuned by changing the dimensions of the probe. The first-order design rule is to reduce the tip mass as much as possible to get a high finger resonance. In addition, we can tune the ratio of sensor resonance frequency to cantilever resonance frequency by adjusting the ratio of grating force sensor finger length to the cantilever beam length. As this ratio decreases, the ratio of sensor to cantilever resonance frequency increases, and therefore, the relative temporal resolution is increased. Moreover, modifying the length of sensor or cantilever does not complicate the fabrication process and therefore it is the preferred way of tuning the relative temporal resolution of our probes.

Increasing the relative temporal resolution by decreasing the length of the grating fingers, however, comes with a cost of increased stiffness, which reduces the sensitivity of the force measurements. Due to this trade-off, sensor sensitivity and its temporal resolution should be optimized for materials with different elasticity. Therefore, we design our probes with a range of different sensor to cantilever beam length ratios so that we can achieve optimum performance on different materials.

Calibrated measurements with the interferometric grating force sensor require knowledge of its complete mechanical transfer function. Accurate measurements and modeling of the spectral response are necessary for calculation of the tip–sample interaction force from differential sensor signals. Therefore, we must know the responses of both moving and reference fingers to the forces acting on the tip and the cantilever beam. In the ideal case, the sensor grating fingers should move relatively only when there is force acting on the tip. In reality, however, the flexural oscillations of the cantilever couple to the differential grating signal. This mechanical coupling is due to unequal responses of the moving and reference fingers to the flexural cantilever oscillations. Specifically, the tip-coupled moving finger set is longer and has a concentrated mass at the end, and therefore, has a lower flexural resonance frequency than the shorter and lighter grating reference fingers. In order to minimize the resulting differences in the spectral responses of the two, the outer fingers of the tip-coupled moving fingers are shortened by incorporating thick support regions around the grating. This increases the stiffness of the moving part and therefore decreases the difference between the resonance frequencies of the moving and reference grating fingers.

The simulated frequency responses of the differential grating sensor with and without balancing are shown in Fig. 1.12. From these figures, we see that balancing minimizes the effect of mechanical coupling of cantilever oscillations into the differential sensor grating signal. The coupling is only significant around the flexural resonances of the cantilever. Consequently, in the balanced case the spectral response of the differential grating sensor can be approximated as a simple harmonic oscillator. The balancing of the sensor has two advantages. First, it eliminates antiresonances in the mechanical response which might cause information loss if the displacement at that frequency is below the detector noise level. Second, it simplifies the experimental characterization of the sensor response to obtain the

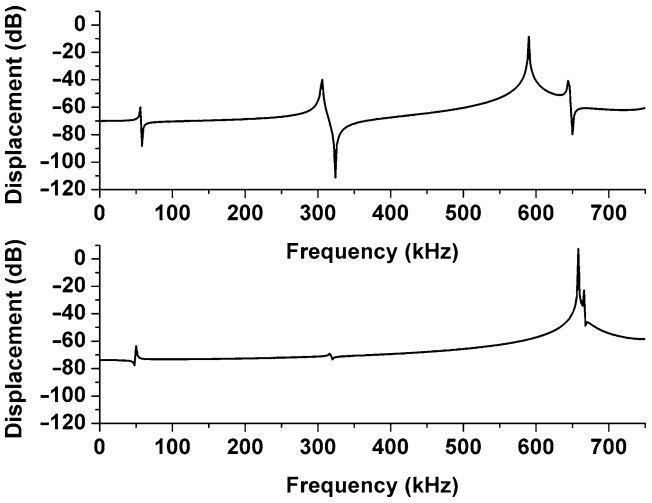

Fig. 1.12 Simulated transfer function of the force sensor without (*upper*) and with (*lower*) the support regions. The support equalizes the resonance frequencies of the moving fingers and the reference fingers and minimizes coupling between the force sensor and the cantilever. Reprinted with permission from [25]. Copyright 2009, IEEE

time-resolved tip–sample interaction force. The entire response can be estimated with the measurement of sensor resonance frequency and quality factor.

1.3.4 Fabrication

The fabrication process is outlined in Fig. 1.13. The probes are fabricated in parallel using optical lithography. The fabrication process starts with a silicon-on-insulator (SOI) wafer (Fig. 1.13a). First, the height offset between the reference and moving grating fingers to ensure maximum force sensitivity is created using Local Oxidation of Silicon (LOCOS). In this process, an 80-nm-thick layer of stoichiometric silicon nitride film is deposited using low pressure chemical vapor deposition (LPCVD) following an oxidation step to grow a 40-nm-thick oxide layer (Fig. 1.13b). This particular combination of film thicknesses ensures that the tensile stress on the silicon nitride film is compensated by the compressive stress in the oxide layer. Next, the silicon nitride layer is etched down to the underlying oxide layer using plasma etching, and then a thermal oxidation at 1,000°C is performed. During this oxidation process, the dense nitride layer acts as a diffusion barrier for oxygen, and therefore, oxidation of the silicon takes place only in the regions that are not covered by the nitride film, i.e., the reference fingers (Fig. 1.13c). The duration of the oxidation step to achieve the correct height offset is determined using the Deal–Grove model [44]. The advantages of using LOCOS instead of plasma etching to pattern the surface

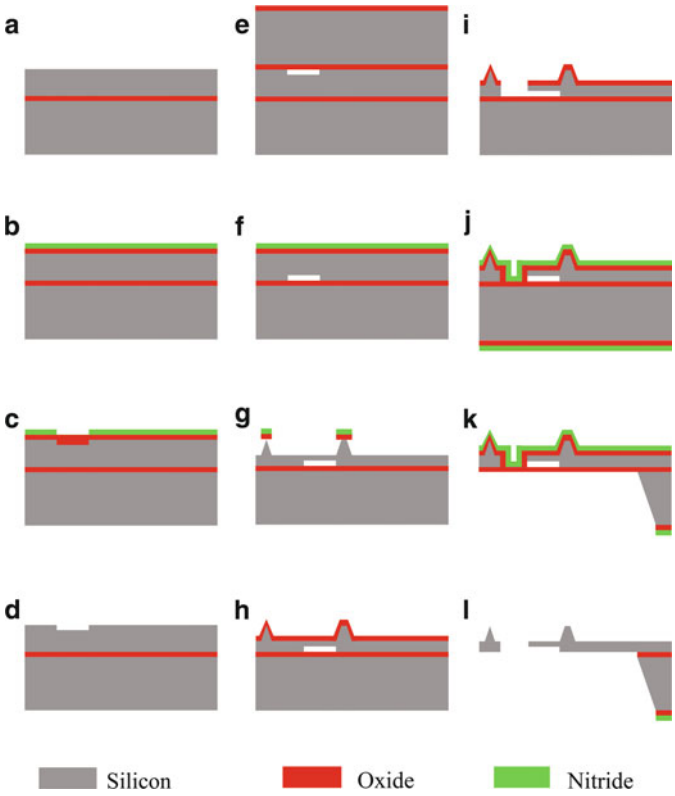

Fig. 1.13 Fabrication process for AFM probes with integrated interferometric high-bandwidth force sensors

are that the LOCOS process provides more accurate etch depth control and also preserves the low surface roughness of the Si wafer, which is crucial for the performance of the interferometric grating sensor. Following the LOCOS step, the silicon nitride film is etched in a phosphoric acid at 150°C and the oxide layer is etched using 6:1 Buffered Oxide Etch (BOE) (Fig. 1.13d).

Next, a double side polished Si wafer with a 1-μm-thick oxide layer is fusion-bonded to the patterned device layer of the SOI wafer. The bonding is performed initially at room temperature and is completed by a wet oxidation at 1,050°C for 2 h (Fig. 1.13e). The oxide layer grown during this step is used as a masking material for the subsequent TMAH etching. First, the oxide layer on the substrate of the original SOI wafer is removed using mechanical grinding and the substrate of the starting SOI wafer is etched in a 20% TMAH solution in water at 95°C. Following the etch, the masking oxide layers are stripped using 6:1 BOE.

Note that at this stage of the process, the height offsets for the grating sensor are buried at the interface between the device layer and buried oxide (BOX) layer of the SOI wafer. Next, a 1-μm-thick oxide film is grown at 1,000°C, followed by the

deposition of 100-nm-thick silicon nitride film using LPCVD (Fig. 1.13f). To create a masking layer for the tip and thick support regions around the grating sensor, the nitride film and the underlying oxide films are etched using plasma etching and in a 6:1 BOE solution, respectively. Following this, the tips and the thick support regions are created by SF_6 based isotropic plasma etching until the oxide/nitride tip masks are released (Fig. 1.13g). Next, the tips are oxide-sharpened at 950°C for 2 h (Fig. 1.13h) [45]. The oxide layer grown in the tip sharpening process is used as a masking layer for ion etching the Si device layer to create the cantilever with the grating sensor (Fig. 1.13i). To protect the probe from the subsequent wet etch, the surface is covered with a 1-μm-thick tetraethyl orthosilicate (TEOS) film and then a 300-nm-thick low-stress LPCVD silicon nitride film is deposited as a masking layer for the next KOH etch (Fig. 1.13j). Before KOH etching, the nitride and oxide masking layers on the backside are patterned using plasma etching and 6:1 BOE, respectively. Next, the Si substrate is etched through the backside nitride mask using a 30% KOH solution at 80°C (Fig. 1.13k). Finally, the probes are released by first etching the nitride layer on the front surface using a plasma etch and stripping the remaining oxide masking films in a 6:1 BOE solution (Fig. 1.13l). An SEM micrograph of the finished probe is shown in Fig. 1.14, and a close-up showing details of the interferometric sensor, including the height offset at the base of the reference fingers, is given in Fig. 1.15.

1.3.5 Detection Schemes

Bending of flexible cantilevers can be detected using various techniques, including the optical lever [46,47], optical interferometers [48,49], and piezoresistive sensors [50]. Due to its simplicity, the most popular is the optical lever, in which a collimated laser beam is reflected from the back of the cantilever to a four-quadrant photodiode. The position of the reflected laser spot on the photodiode changes due to flexural or torsional bending of the cantilever beam. Resulting vertical and lateral changes

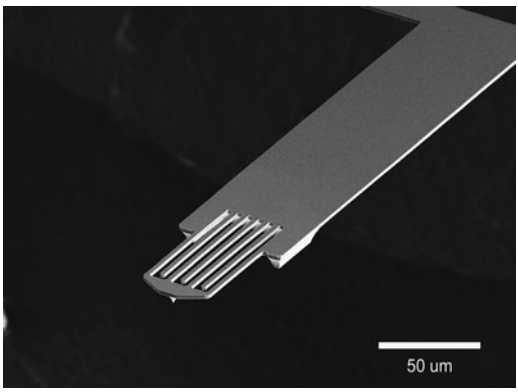

Fig. 1.14 SEM micrograph of an AFM probe with integrated interferometric high-bandwidth force sensor. Reprinted with permission from [25]. Copyright 2009, IEEE

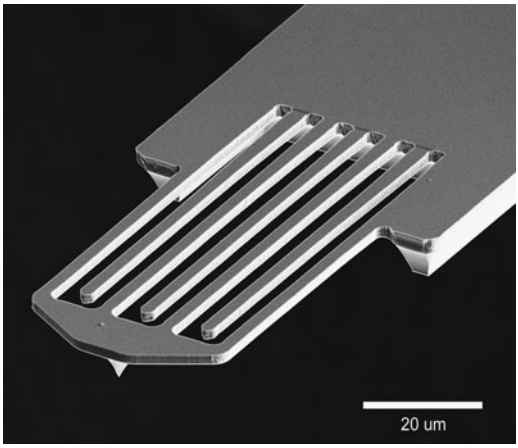

Fig. 1.15 Close-up of the high-bandwidth force sensor. Reprinted with permission from [25]. Copyright 2009, IEEE

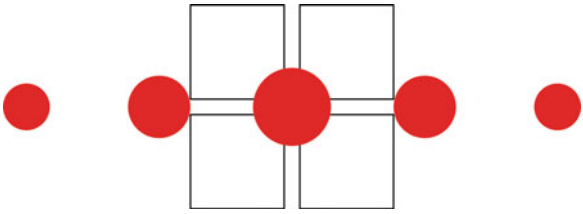

Fig. 1.16 Alignment of diffracted orders (*red circles*) on the built-in AFM quadrant photodiode. In this setting, the vertical position gives the cantilever displacement, and the total light intensity gives the sensor displacement and force

in the laser spot position are obtained by measuring the light intensity difference between the top/bottom and left/right halves of the four-quadrant photodiode.

There are two ways to operate our probes using a single focused laser beam and the built-in four-quadrant photodiode in a conventional AFM system that employs optical lever detection. In the first method, one of the diffracted laser spots is placed at the center of the quadrant photodiode as shown in Fig. 1.16. The other spots can either be left out of the active area if the size of the photodiode is small enough or they can be blocked using an aperture. In this configuration, the flexural oscillations of the cantilever cause the diffracted laser spot to move in the vertical direction and are measured by tracking the position of the diffracted laser spot using the vertical difference signal of the four-quadrant photodiode. For interaction force measurements, the relative tip displacement with respect to the cantilever can be simultaneously measured by changes in the total light intensity of the diffracted spot by adding the outputs of all the individual cells of the four-quadrant diode.

The second approach requires the two adjacent diffracted laser spots to be placed onto the left and right halves of the four-quadrant photodiode as shown in Fig. 1.17. Note that the spots are placed such that they are vertically centered. In this setting, the flexural oscillations of the cantilever can be measured by detecting the

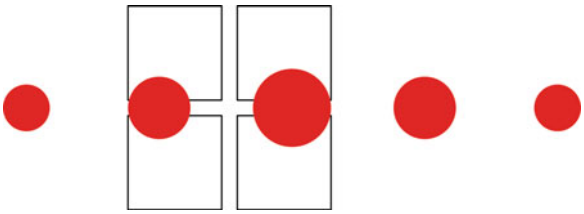

Fig. 1.17 Alignment of diffracted orders (*red circles*) on the built-in AFM quadrant photodiode. In this setting, the vertical position gives the cantilever displacement, and the lateral difference in intensity gives the sensor displacement and force

collective vertical displacement of the two adjacent diffracted spots. Similar to the first method, this is accomplished by using the vertical difference signal of the four-quadrant photodetector. On the other hand, the relative tip displacement with respect to the cantilever is simultaneously detected by measuring the difference in the light intensities of the two adjacent diffracted orders. This is simply achieved by using lateral difference output of the four-quadrant phototodetector.

The power of these detection techniques is that they provide simultaneous measurements of the flexural cantilever displacement and the relative tip–cantilever displacement. Both the detection techniques are combinations of optical lever and interferometry, yet they use AFM's own laser diode, built-in four-quadrant photodiode and already available standard output signals for common AFM operating modes. In addition, both techniques enable independent measurements of the tip and cantilever displacements because the positions and the intensities of the diffracted spots are orthogonal parameters that do not affect each other.

Despite their similarities, the two measurement modes are distinct in terms of their ease of use and noise performance. In particular, the first method that uses a single diffracted laser spot is simpler to implement in practice since it does not impose any extra limitations on the size of the photodiode. However, in this method, the relative tip displacement measurements are affected by laser instabilities since the intensity fluctuations of the laser diode output are directly coupled to the intensity measurements of the spot. This issue is not as significant in the second method since the differential measurement of light intensities of two spots minimizes common mode noise due to laser diode intensity and wavelength instabilities. In addition, a dark zone between the two spatially separated diffraction modes on the photodiode eliminate possible crosstalk between vertical and lateral signals in tapping-mode operation that might occur due to the misalignment between the cantilever and photodiode axes. From practical point of view, the second method requires more specialized design, because the four-quadrant photodiode must be large enough that each lateral half can accommodate a single diffracted spot. This means that the photodiode is designed for a specific probe-to-photodiode distance and cantilever geometry.

1.3.6 Characterization and Calibration

The fabricated probes are characterized in an AFM system by measuring the static and dynamic responses of the grating force sensor. In these measurements, a focused laser beam is positioned on the grating force sensor and the zeroth and first diffracted spots are placed on the four-quadrant photodiode as explained in the previous section.

To characterize the grating sensor response for large displacements and to confirm the initial height offset in the fabricated devices, we use a grating force sensor test structure with 200-μm long interdigitated fingers directly attached to a substrate. By driving the AFM piezoelectric actuator with a triangular waveform, the tip of test structure is pushed in and out of a hard surface at a rate of 100 Hz and the specular reflection intensity is recorded. In this experiment, the dynamic response of the fingers can be neglected since the sensor resonance frequencies are much higher than 100 Hz. Figure 1.18 shows the reflected light intensity modulation recorded in one of the approach/retract cycles of the grating sensor test structure. In this measurement, tip–sample contact occurs at $t = 0.5$ ms and the tip is pushed into the sample until $t = 2$ ms. Then the tip is pulled away and it loses contact with the surface at $t = 3.75$ ms. The asymmetry between the approach and retract phases is due to hysteresis in the tip–sample contact, which is likely a result of a water meniscus between the tip and sample. Specifically, from $t = 3.3$ ms to $t = 3.75$ ms, the tip is pulled by the sample and the fingers are displaced in the opposite direction. This effect is useful for characterization purposes, because it enables observations of the optical response due to attractive forces. In Fig. 1.18, right after the tip-contact at $t = 0.5$ms, the light intensity of the zeroth order decreases in an approximately

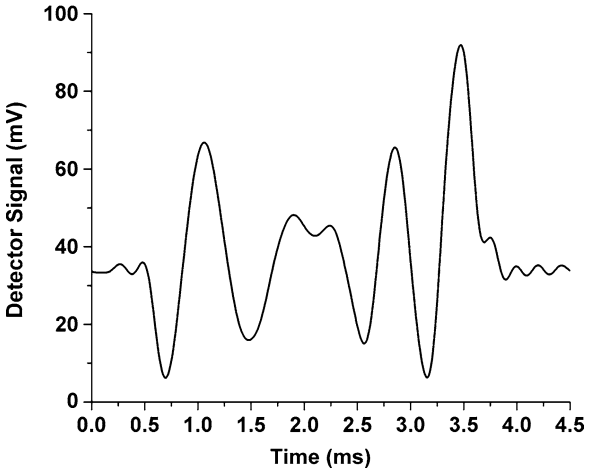

Fig. 1.18 Reflected intensity as the sensor is pushed down and pulled back from surface with a piezoelectric actuator at a rate of 100 Hz. Reprinted with permission from [25]. Copyright 2009, IEEE

linear dependence on the finger displacement. This observation confirms the initial height offset in the fabricated devices, because an unbiased grating sensor would be insensitive to the grating finger displacements at the point of contact [from (1.24)]. Using the retract portion of the results in Fig. 1.18, the initial height offset in the fabricated force sensor is found to be 93.2 nm. The calculated optimum bias that includes the effect of 10° cantilever tilt is 85 nm. Therefore, these results also confirm the initial height offset and show that the fabricated devices are biased close to optimum.

Figure 1.18 also shows that the modulation index of the reflected light is decreasing with the increasing finger displacement. This effect is due to curvature of the grating fingers with the increasing tip displacement. This does not create a problem for our measurements, because under normal TM-AFM imaging conditions, the sensor grating fingers displace less than a nanometer, given that the peak tip–sample forces do not exceed a few of tens of nanonewtons.

To calibrate the photodetector output for force measurements, the probe is engaged on a hard surface and the tip–sample force is modulated by modulating the calibrated AFM piezoelectric actuator with a triangular waveform. The force acting on the tip is calculated by multiplying the probe (cantilever and the force sensor combined) spring constant and the piezoactuator displacement. In this process, the probe spring constant is determined by the thermal tune method [51, 52]. To calibrate the photodetector output for quantitative force measurements, the output signal is measured for a specific tip–sample interaction force and the conversion parameter is calculated. Note that this parameter not only depends on the probe properties but also depends on the specifications of the AFM photodetector, i.e., the photodiode responsivity and transimpedance gain of the photodetector circuit.

Finally, to characterize the dynamic response of the grating sensor, we measure its step response and determine its resonance frequency and quality factor. This is achieved by recording the photodetector signal as the tip goes in and out of contact with a sample. Under ambient conditions, sample surfaces are covered with a thin layer of water, so the tip–sample rupture due to breaking of the capillary neck effectively presents a force step function on the tip. From these measurements, the grating sensor resonance frequency and its quality factor are calculated by measuring the frequency and the decay time of the sensor ringing oscillations, respectively.

1.3.7 Time-Resolved Force Measurements

In this section, we demonstrate the operation of our probes in tapping mode and present force measurement results. In these measurements, the probe is driven close to its fundamental resonance by a piezoactuator from its base and the cantilever oscillations and relative tip motion are measured by observing the location and intensity of the two adjacent diffracted spots on a four-quadrant photodetector as explained before.

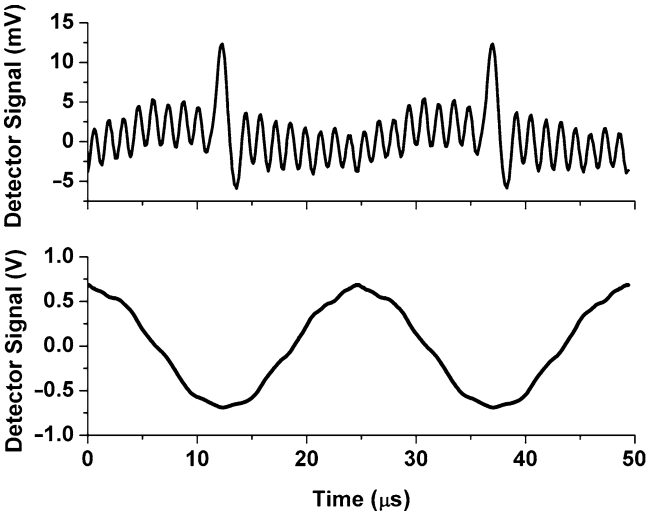

Fig. 1.19 Oscilloscope traces for tip (*upper*) and cantilever (*lower*) displacement. Reprinted with permission from [25]. Copyright 2009, IEEE

Figure 1.19 shows oscilloscope traces of cantilever motion and relative tip displacement signals measured as the probe periodically interacts with the same location on a sample. The measurements clearly show that the tip–sample interactions are time-resolved from the tip-displacement signal. Moreover, the force measurements are in agreement with the cantilever displacement signal, because tip–sample forces are measured only when the cantilever is close to the sample surface as expected. Note that the time-resolved force signals also show hysteresis in the tip–sample interaction due to larger adhesive force during tip retraction. The measurements also show that the cantilever trajectory remains close to sinusoidal, with small distortions due to the higher harmonics introduced by the tip–sample interaction. In the specific probe of Fig. 1.19, the cantilever beam is 250-μm long, 60-μm wide and 2.5-μm thick, and the grating fingers are 70-μm long, 3-μm wide and 2.5-μm thick. This geometry leads to a grating-sensor resonance frequency that is approximately 18 times the cantilever fundamental resonance frequency. The ringing oscillations present in the tip displacement signal are due to the vibrations of the high-bandwidth force sensor with a frequency close to its fundamental resonance frequency. These are triggered by the higher harmonics of the tip–sample interaction. The ringing decays very little between the consecutive tapping events, indicating a high quality factor of the force sensor in air, consistent with the results of our analysis in Sect. 1.3.1.

In order to perform quantitative force measurements, the grating sensor signal should be processed to compensate the frequency response of the grating sensor. For this purpose, the sampled grating sensor signal is filtered using the inverse of the estimated transfer function of the force sensor in the previous section [15,16]. In this process, a cut-off frequency is introduced in the calculations to prevent divergence

above the resonance frequency. This inverse filtering cancels the effect of nonuniform mechanical gain of the grating sensor, and therefore removes the ringing due to the resonance. However, after this step the processed waveform may still be distorted due to several nonidealities such as nonlinear photodiode response and coupling of cantilever flexural resonances to the grating signal. To remove these effects, we use the assumption that the tip–sample interaction force should be close to zero except at times close to the tip–sample contact. Therefore, the contributions of the nonidealities are approximated by using a curve fitting algorithm based on least-squares method. For this curve fitting process, the harmonics of the cantilever drive signal are used as the basis set. This procedure is only applied on the parts of the waveform, in which the tip and sample are not expected to be in contact. By subtracting the estimated fit from the original, a corrected waveform is obtained. Finally, the calibration parameters measured with the procedures outlined in the previous section,

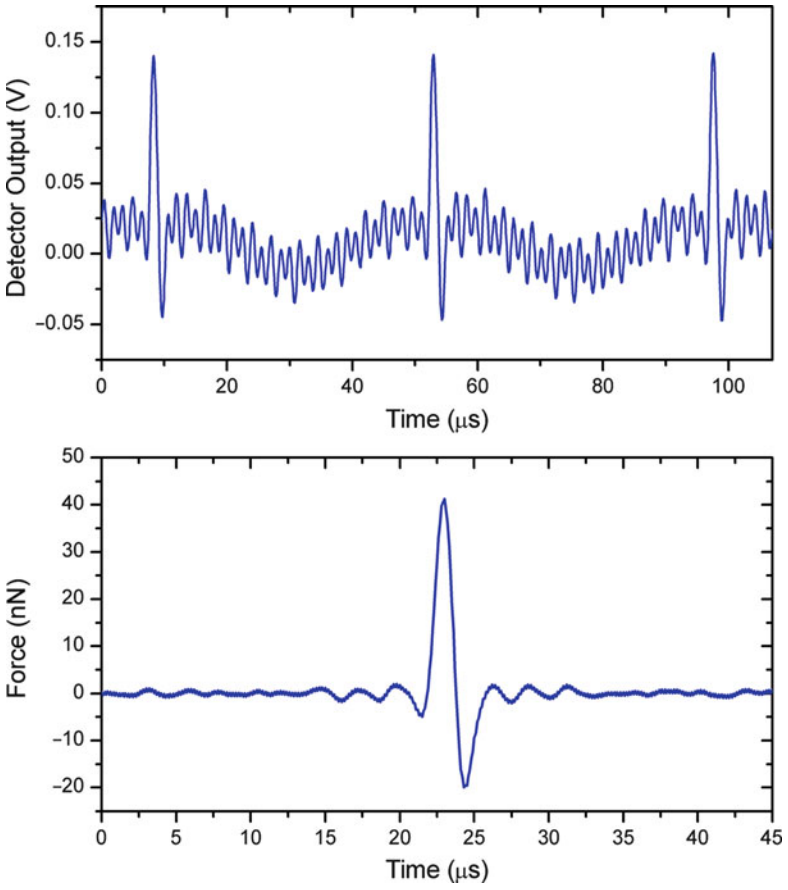

Fig. 1.20 Raw (*top*) and processed (*bottom*) force signals acquired during TM-AFM imaging of a Si sample. Reprinted with permission from [24]. Copyright 2008, American Institute of Physics

are used to convert the photodetector output into force values. Figure 1.20 shows the interaction–force waveform before and after this signal processing has been carried out. These measurements were performed on a Si sample in ambient conditions using a probe with a force sensor that has 30 times higher mechanical bandwidth than the cantilever.

1.4 Imaging Applications

In previous sections, we introduced and analyzed an AFM probe that can resolve tip–sample interaction forces during TM-AFM imaging. We showed that these probes can resolve tip–sample interaction with high temporal resolution and can be used in standard AFM systems without requiring excessive modifications. In this section, we use these probes to form images that are based on time-resolved tip–sample force measurements. First, the imaging technique and experimental setup is explained, and imaging results on composite surfaces, including block copolymers and SAMs of alkanethiols are presented.

As discussed in Sect. 1.2.2, the spectrum of the periodic and nonlinear interaction force waveform in TM-AFM contains harmonics at the integer multiples of the cantilever drive frequency. Therefore, a simple way to create AFM images based on the tip–sample interaction force information is to record the amplitude of one of the higher harmonics of the quasi-periodic force signal [17, 53]. A schematic of our imaging setup is shown in Fig. 1.21. Higher harmonic imaging experiments are done using a commercial AFM system. The AFM's built-in 670 nm laser diode and the four-quadrant photodetector are used for detection of the diffraction spots that

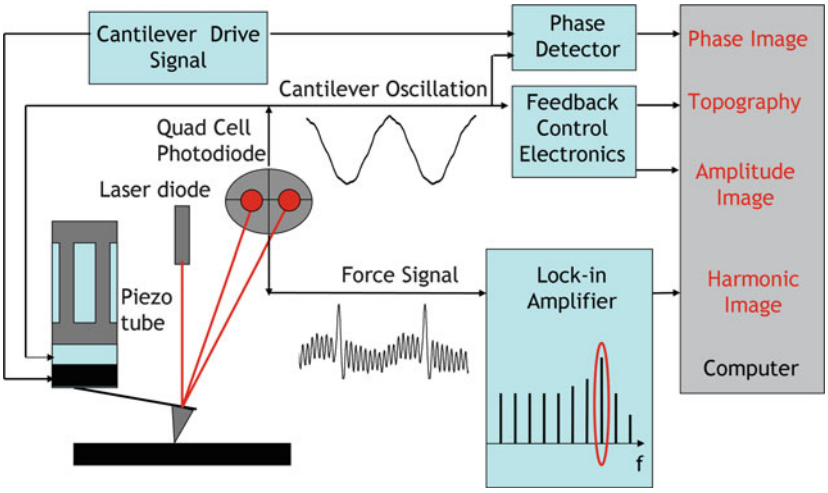

Fig. 1.21 Schematic of experimental setup used for harmonic imaging

are aligned on the photodetector as explained in Sect. 1.3.5. The cantilever oscillation and the force signals are obtained from the vertical and lateral differential channels of the photodetector. In operation, the feedback to the piezoelectric actuator is set to keep a constant cantilever oscillation amplitude, and a lock-in amplifier is used to measure the signal power of one specific higher harmonics of the force signal. To achieve this, two signal generators sharing a common time base are used. The first one is used to drive the cantilever close to its fundamental resonance frequency. The second one is used to generate the reference harmonic signal for the lock-in amplifier. The frequency of this signal is an integer multiple of the cantilever drive frequency. The specific imaging harmonic is simply chosen by adjusting the frequency of the reference signal. In our experiments, we use the harmonic in the vicinity of the grating sensor resonance in order to benefit from the improved sensitivity due to resonance enhancement.

Harmonic imaging using our probes provides advantages over applying the same technique with a regular AFM probe. In the cantilever displacement spectrum, only harmonics that are close to flexural resonances of the cantilever are recovered [17], whereas the force sensor signal can provide a full spectrum harmonics due to larger mechanical bandwidth of the force sensor. Our probes provide freedom to choose a specific harmonic from a range of harmonics to obtain the optimum material contrast and enables simultaneous images of several harmonics.

1.4.1 Nanomechanical Material Mapping

To demonstrate the material mapping capabilities of our probes, we tested our probes on a control sample that we prepared by using focused ion beam-assisted material deposition on a Si surface. In this sample, 150 nm high $1 \times 1\,\mu$m Pt and TEOS islands are deposited in a 5×5 checkerboard pattern. In imaging this sample, the probe is driven close to its resonance frequency at 44.16 kHz and the spectral component at 441.6 kHz is recorded using lock-in detection to create the 10th harmonic image.

Figure 1.22 shows the simultaneously captured topography, amplitude, phase, and 10th harmonic images of the checkerboard test sample. In the 10th harmonic image, the Pt and TEOS islands are clearly distinguishable so that the checkerboard deposition pattern is revealed. The contrast in the harmonic image is due to the fact that the tip–sample interaction waveform in TM-AFM is affected by the local mechanical properties of the sample. From the conventional TM-AFM images in Fig. 1.22, we see that the checkerboard pattern is also apparent in the topography and phase image. However, the contrast mechanism of the topography image is the physical topographical properties of the surface. For this particular sample, the topography image indicates that the Pt islands are higher in topography compared to TEOS islands. The phase image contrast in TM-AFM is created by inelastic tip–sample interactions [54]. Therefore, the phase image of Fig. 1.22 indicates that the average dissipated energy on the two material surfaces is different. This shows that our imaging modality adds information to that obtained by the traditional imaging methods.

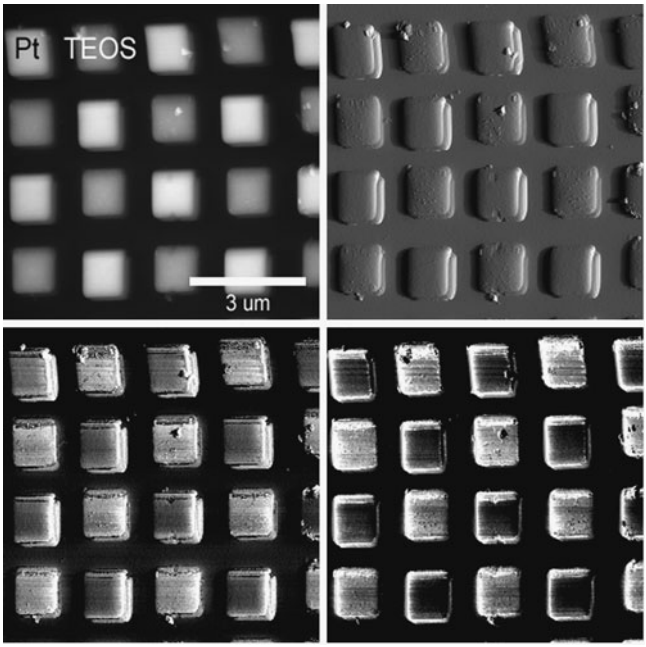

Fig. 1.22 Topography (*upper-left*), amplitude (*upper-right*), phase (*lower-left*) and 10th harmonic (*lower-right*) images of the checkerboard test sample. Reprinted with permission from [25]. Copyright 2009, IEEE

1.4.2 Imaging of Molecular Structures in Self Assembled Monolayers

The nanoscale structure of molecules has strong effects on their mechanical properties. In this section, we demonstrate that our probes can discriminate between two distinct structural forms of the same molecule through changes in its mechanical properties. In this experiment, the sample is a self assembled monolayer (SAM) of C_{18} molecules on a gold-coated mica surface.

Formation of SAM alkanethiols on surfaces has been a subject of several studies [55, 56]. These studies show that during the formation of alkanethiol SAMs, the head groups adsorb on the surface quickly to minimize their free energy. These molecules are initially in a noncrystalline state called the lying-down state. Over time the molecules pack more closely to form a crystalline state called the standing-up state. The ratio of the two structural states on the gold surface depends on the time that the gold surface is exposed to the solution containing $C_{18}SH$ molecules during sample preparation.

During sample preparation, the exposure time is adjusted such that the sample is covered with both lying-down and standing-up states. A 500×500 nm area of this sample is scanned as the probe is driven at 40.5 kHz and amplitude of the 18th harmonic of the force sensor signal is recorded to obtain the harmonic image.

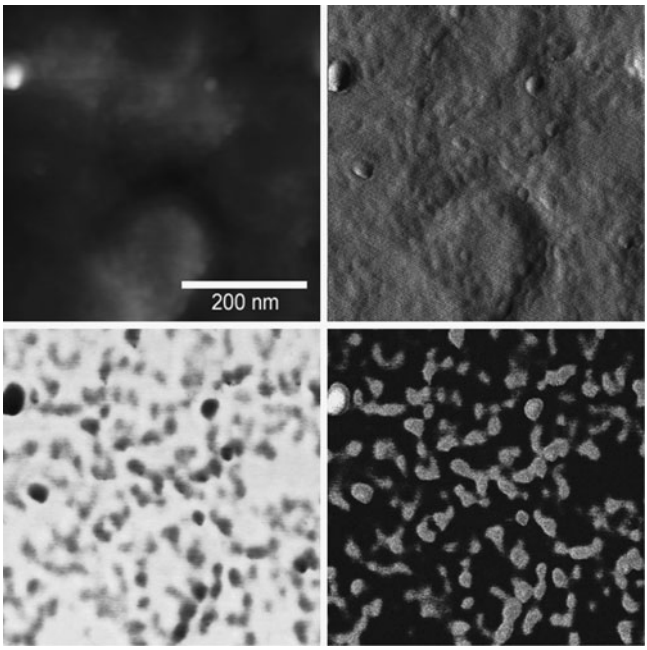

Fig. 1.23 Topography (*upper-left*), amplitude (*upper-right*), phase (*lower-left*) and 18th harmonic (*lower-right*) images of C_{18} self assembled monolayer on gold. Reprinted with permission from [25]. Copyright 2009, IEEE

Figure 1.23 shows the topography, amplitude, phase, and 18th harmonic images of the gold surface covered with both vertical and horizontal C_{18} molecules. The height difference between the two molecular states is too small to be clearly seen in the topography image. The amplitude image, being sensitive to topography gradients, shows the boundaries between the two states. From the harmonic image, we see that the two different states of the C_{18} molecules are clearly distinguished. This is an expected result since the structural properties of the molecules and their packing density are closely related to their mechanical properties. Also note that the results from harmonic image are in qualitative agreement with the phase image, even though the contrast mechanisms are vastly different.

1.4.3 Imaging Microphase Seperation in Triblock Copolymer

We also used thin block copolymer films to demonstrate the nanomechanical mapping capability of our probes. AFM and its related techniques are widely used for studying polymer surfaces [57]. Block copolymers are particularly interesting since they are composed of different polymer subunits and they form nanostructures with varying mechanical properties on the nanoscale [58].

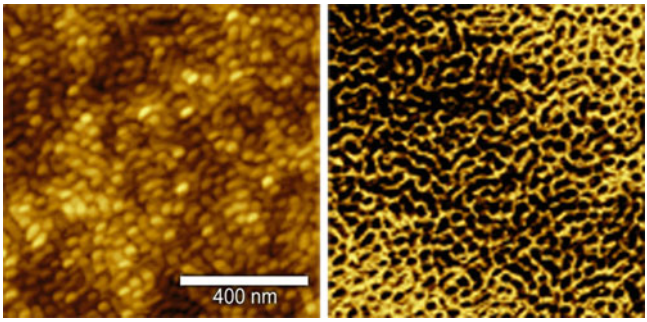

Fig. 1.24 Topography (*left*) and simultaneously acquired 17th harmonic image (*right*) of thin film of SBS triblock copolymer (Scan size: $1 \times 1\ \mu m$). Reprinted with permission from [24]. Copyright 2008, American Institute of Physics

Our sample in this experiment is a triblock copolymer, namely, SBS. This polymer is formed by repeating polystyrene, polybutadiene, and polystyrene polymer blocks, with a periodicity on the order of 40–50 nm [59]. At room temperature, the polybutadiene blocks are above their glass transition temperature, and hence are in rubbery state, whereas the polystyrene blocks are below their glass transition temperature and are in glassy state. This contrast in the elastic properties of the polymer blocks at room temperature makes the SBS polymer an interesting sample for mapping of surface elasticity. Figure 1.24 shows topography and 17th harmonic of the sample. The 17th harmonic image clearly shows the microphase separation between the two subunits. The bright and dark regions in the 17th harmonic image correspond to stiff polystyrene and compliant polybutadiene blocks, respectively.

1.5 Conclusion

In this chapter we present a technique for quantitative nanoscale analysis of materials based on the time-resolved measurement of tip–sample interaction forces in TM-AFM. The technique combines the advantages of TM-AFM imaging, namely nondestructive, high resolution, and fast operation, with the quantitative force-measurement capabilities of static AFM force measurement methods. This development therefore transforms TM-AFM from a technique useful primarily for physical topography measurements to a tool for quantitative material analysis with high sensitivity and resolution, giving it the potential for solving a wide range of measurement problems in material science, biology and medicine.

References

1. G. Binnig, C.F. Quate, C. Gerber, Atomic force microscope. Phys. Rev. Lett. **56**, 930 (1986)
2. F.J. Giessibl, S. Hembacher, H. Bielefeldt, J. Mannhart, Subatomic features on the silicon (111)-(7 × 7) surface observed by atomic force microscopy. Science **289**, 422 (2000)
3. N.A. Burnham, R. J. Colton, Measuring the nanomechanical properties and surface forces of materials using an atomic force microscope. J. Vac. Sci. Technol. A **7**, 2906 (1989)
4. M. Radmacher, J.P. Cleveland, M. Fritz, H.G. Hansma, P.K. Hansma, Mapping interaction forces with the atomic force microscope. Biophys. J. **66**, 2159 (1994)
5. K. Yamanaka, H. Ogiso, O. Kolosov, Ultrasonic force microscopy for nanometer resolution subsurface imaging. Appl. Phys. Lett. **64**, 178 (1994)
6. O.V. Kolosov, M.R. Castell, C.D. Marsh, G.A.D. Briggs, T.I. Kamins, R.S. Williams, Imaging the elastic nanostructure of Ge Islands by ultrasonic force microscopy. Phys. Rev. Lett. **81**, 1046 (1998)
7. A. Rosa-Zeiser, E. Weilandt, S. Hild, O. Marti, The simultaneous measurement of elastic, electrostatic and adhesive properties by scanning force microscopy: pulsed-force mode operation. Meas. Sci. Technol. **8**, 1333 (1997)
8. H. Krotil, T. Stifter, H. Waschipky, K. Weishaupt, S. Hild, O. Marti, Pulsed force mode: a new method for the investigation of surface properties. Surf. Interface Anal. **27**, 336 (1999)
9. P. Maivald, H.J. Butt, S.A.C. Gould, C.B. Prater, B. Drake, J.A. Gurley, V.B. Elings, P.K. Hansma, Using force modulation to image surface elasticities with the atomic force microscope. Nanotechnology **2**, 103 (1991)
10. M. Radmacher, R.W. Tillmann, H.E. Gaub, Imaging viscoelasticity by force modulation with the atomic force microscope. Biophys. J. **64**, 735 (1993)
11. Q. Zhong, D. Inniss, K. Kjoller, V.B. Elings, Fractured polymer/silica fiber surface studied by tapping mode atomic force microscopy. Surf. Sci. **290**, 688 (1993)
12. C. Moller, M. Allen, V. Elings, A. Engel, D.J. Muller, Tapping-mode atomic force microscopy produces faithful high-resolution images of protein surfaces. Biophys. J. **77**(2), 1150–1158 (1999)
13. D.A. Chernoff, *Proceedings of Microscopy and Microanalysis 1995* (Jones and Begell, New York, 1995)
14. S.N. Magonov, V. Elings, V. S. Papkov, AFM study of thermotropic structural transitions in poly(diethylsiloxane). Polymer **38**, 297 (1997)
15. M. Stark, R.W. Stark, W.M. Heckl, and R. Guckenberger, Inverting dynamic force microscopy: From signals to time-resolved interaction forces. PNAS **99**, 8473 (2002)
16. J. Legleiter, M. Park, B. Cusick, T. Kowalewski, Scanning probe acceleration microscopy (SPAM) in fluids: Mapping mechanical properties of surfaces at the nanoscale. PNAS **103**, 4813 2006)
17. O. Sahin, G. Yaralioglu, R. Grow, S.F. Zappe, A. Atalar, C.F. Quate, O. Solgaard, High resolution imaging of elastic properties using harmonic cantilevers. Sens. Actuators A **114**, 183 (2004)
18. S. Sadewasser, G. Villanueva, J.A. Plaza, Special cantilever geometry for the access of higher oscillation modes in atomic force microscopy. Appl. Phys. Lett. **89**, 033106 (2006)
19. R. Proksch, Multifrequency, repulsive-mode amplitude-modulated atomic force microscopy. Appl. Phys. Lett. **89**, 113121 (2006)
20. A.G. Onaran, M. Balantekin, W. Lee, W.L. Hughes, B.A. Buchine, R.O. Guldiken, Z. Parlak, C.F. Quate, F.L. Degertekin, A new atomic force microscope probe with force sensing integrated readout and active tip. Rev. Sci. Instrum. **77**, 023501 (2006)
21. M. Balantekin, A.G. Onaran, F.L. Degertekin, Quantitative mechanical characterization of materials at the nanoscale through direct measurement of time-resolved tip-sample interaction forces. Nanotechnology **19**, 085704 (2008)
22. O. Sahin, S. Magonov, C. Su, C.F. Quate, O. Solgaard, An atomic force microscope tip designed to measure time-varying nanomechanical forces. Nat. Nanotechnol. **2**, 507 (2007)

23. O. Sahin, N. Erina, High-resolution and large dynamic range nanomechanical mapping in tapping-mode atomic force microscopy. Nanotechnology **19**, 445717 (2008)
24. A.F. Sarioglu, O. Solgaard, Cantilevers with integrated sensor for time-resolved force measurement in tapping-mode atomic force microscopy. Appl. Phys. Lett. **93**, 023114 (2008)
25. A.F. Sarioglu, M. Liu, O. Solgaard, Interferometric force sensing AFM probes for nanomechanical mapping of material properties, in *Proceedings of the 15th International Conference on Solid-State Sensors, Actuators and Microsystems – IEEE Transducers*, Denver, CO, USA, 2009, pp. 1634–1637
26. R. Garcia, A. San Paulo, Attractive and repulsive tip-sample interaction regimes in tapping-mode atomic force microscopy. Phys. Rev. B **60**, 4961 (1999)
27. J. Israelachvili, *Intermolecular and Surface Forces* (Academic, London, 2003)
28. B.V. Derjaguin, V.M. Muller, Y.P. Toporov, Effect of contact deformations on the adhesion of particles. J. Colloid Interface Sci. **53**, 314 (1975)
29. L.D. Landau, E.M. Lifshitz, *Theory of Elasticity* (Pergamon, New York, 1986)
30. J. Tamayo, R. Garcia, Deformation, contact time, and phase contrast in tapping mode scanning force microscopy. Langmuir **12**, 4430 (1996)
31. A.S. Paulo, R. Garcia, Unifying theory of tapping mode atomic force microscopy. Phys. Rev. B **66**, 041406 (2002)
32. A.S. Paulo, R. Garcia, Tip-surface forces, amplitude, and energy dissipation in amplitude modulation (tapping mode) force microscopy. Phys. Rev. B. **64**, 193411 (2001)
33. J. Chen, R.K. Workman, D. Sarid, R. Hoper, Numerical simulations of a scanning force microscope with a large-amplitude vibrating cantilever. Nanotechnology **5**, 199 (1994)
34. S.I. Lee, S.W. Howell, A. Raman, R. Reifenberger, Nonlinear dynamics of microcantilevers in tapping mode atomic force microscopy: A comparison between theory and experiment. Phys. Rev. B **66**, 115409 (2002)
35. T.R. Rodriguez, R. Garcia, Tip motion in amplitude modulation (tapping-mode) atomic-force microscopy: Comparison between continuous and point-mass models. Appl. Phys. Lett. **80**, 1646 (2002)
36. O. Sahin, A. Atalar, Analysis of tip-sample interaction in tapping-mode atomic force microscope using an electrical circuit simulator. Appl. Phys. Lett. **78**, 2973 (2001)
37. M. Balantekin, A. Atalar, Power dissipation analysis in tapping-mode atomic force microscopy. Phys. Rev. B **67**, 193404 (2003)
38. O. Solgaard, F.S.A. Sandejas, D.M. Bloom, Deformable grating optical modulator. Opt. Lett. **17**, 688 (1992)
39. S.R. Manalis, S.C. Minne, A. Atalar, C.F. Quate, Interdigital cantilevers for atomic force microscopy. Appl. Phys. Lett. **69**, 3944 (1996)
40. G.G. Yaralioglu, A. Atalar, S.R. Manalis, C.F. Quate, Analysis and design of an interdigital cantilever as a displacement sensor. J. Appl. Phys. **83**, 7405 (1998)
41. R.J. Bell, *Introductory Fourier Transform Spectroscopy* (Academic, New York, 1972)
42. O. Solgaard, *Photonic Microsystems*, Chapter 10.5 (Springer, Heidelberg, 2009)
43. O. Sahin, A. Atalar, C.F. Quate, O. Solgaard, Resonant harmonic response in tapping-mode atomic force microscopy. Phys. Rev. B. **69**, 165416 (2004)
44. B.E. Deal, A.S. Grove, General Relationship for the Thermal Oxidation of Silicon. J. Appl. Phys. **36**, 3770 (1965)
45. T.S. Ravi, R.B. Marcus, D. Liu, Oxidation sharpening of silicon tips. J. Vac. Sci. Technol. B **9**, 2733 (1991)
46. G. Meyer, N.M. Amer, Novel optical approach to atomic force microscopy. Appl. Phys. Lett. **53**, 1045 (1988)
47. S. Alexander, L. Hellemans, O. Marti, J. Schneir, V. Elings, P.K. Hansma, M. Longmire, J. Gurley, An atomic-resolution atomic-force microscope implemented using an optical lever. J. Appl. Phys. **65**, 164 (1989)
48. Y. Martin, C.C. Williams, H.K. Wickramasinghe, Atomic force microscope-force mapping and profiling on a sub 100-Å scale. J. Appl. Phys. **61**, 4723 (1987)
49. D. Rugar, H.J. Mamin, P. Guethner, Improved fiber-optic interferometer for atomic force microscopy. Appl. Phys. Lett. **55**, 2588 (1989)

50. M. Tortonese, R.C. Barrett, C.F. Quate, Atomic resolution with an atomic force microscope using piezoresistive detection. Appl. Phys. Lett. **62**, 834 (1993)
51. J.L. Hutter, J. Bechhoefer, Calibration of atomic-force microscope tips. Rev. Sci. Instrum. **64**, 1868 (1993)
52. B. Ohler, Cantilever spring constant calibration using laser Doppler vibrometry. Rev. Sci. Instrum. **78**, 063701 (2007)
53. R.W. Stark, W.M. Heckl, Higher harmonics imaging in tapping-mode atomic-force microscopy. Rev. Sci. Instrum. **74**, 5111 (2003)
54. J.P. Cleveland, B. Anczykowski, A.E. Schmid, V.B. Elings, Energy dissipation in tapping-mode atomic force microscopy. Appl. Phys. Lett. **72**, 2613 (1998)
55. G.E. Poirier, E.D. Pylant, The self-assembly mechanism of alkanethiols on Au(111). Science **272**, 1145 (1996)
56. M. Liu, N.A. Amro, G. Liu, Nanografting for surface physical chemistry. Annu. Rev. Phys. Chem. **59**, 367 (2008)
57. S.N. Magonov, D.H. Reneker, Characterization of polymer surfaces with atomic force microscopy. Annu. Rev. Mater. Sci. **27**, 175 (1997)
58. L. Leibler, Theory of microphase separation in block copolymers. Macromolecules **13**, 1602 (1980)
59. S.N. Magonov, J. Cleveland, V. Elings, D. Denley, M.-H. Whangbo, Tapping-mode atomic force microscopy study of the near-surface composition of a styrene-butadiene-styrene triblock copolymer film. Surf. Sci. **389**, 201 (1997)

Springer

http://www.springer.com/978-3-642-10496-1

Scanning Probe Microscopy in Nanoscience and Nanotechnology 2

Bhushan, B. (Ed.)
2011, XXVI, 816 p., Hardcover
ISBN: 978-3-642-10496-1